FORMATION OF OH RADICALS AS EVIDENCE
OF INTRAMOLECULAR HYDROGEN MIGRATION
IN CATION-INDUCED DISSOCIATION OF FURAN MOLECULES

TOMASZ J. WASOWICZ

Division of Complex Systems Spectroscopy, Institute of Physics and Applied Computer Science,
Faculty of Applied Physics and Mathematics, Gdansk University of Technology,
ul. G. Narutowicza 11/12, 80-233 Gdańsk, Poland
E-mail: tomasz.wasowicz1@pg.edu.pl

Abstract. We present the experimental results on a hydrogen atom migration preceding fragmentation of the furan molecules induced by the H_3^+ and C^+ impact. The excited $OH(A^2\Sigma^+)$ radical has been detected among the furan decomposition products using collision-induced emission spectroscopy. However, the OH moiety is absent in the furan ring skeleton, so detecting the $OH(A^2\Sigma^+ \rightarrow X^2\Pi)$ luminescence indicates the intramolecular H atom relocation prior to cation-induced fragmentation. Guided by the most recent theoretical calculations, the dissociation mechanism that governs the $OH(A^2\Sigma^+)$ formation observed in this work is elucidated.

Key words: Hydrogen migration, dissociation, collisions, furan.

1. INTRODUCTION

In scientific, technological, and medical applications, we often encounter the problem of the interaction of various forms of radiation with matter. As a result of this interaction, we observe macroscopic effects to which processes at the microscopic level contribute. Among the most important reactions are excitations, ionizations, and fragmentations of the building blocks of chemical compounds. The bonds rupture in those molecules is often preceded by isomerization associated with the movement of hydrogen atoms or protons along the molecule's backbone. Such a chemical bond rearrangement opens new reaction pathways that molecules cannot usually realize in their primary molecular geometries, see, *e.g.* [1–6]. Optical [7] and free-electron [1, 8] laser experiments and ion-induced fragmentation studies [9] find that hydrogen migrates on a femtosecond timescale and is faster than molecular bond cleavage in dissociation. Thus it may provide selective control [10] over new chemical bond formation or bond scission in radiation damage to biomolecules [11–13], combustion [14], and catalytic reactions [15].

The chemical compounds involved in these reactions are predominantly based on heterocyclic molecules. One such basic heterocycle is the furan molecule (C_4H_4O). Its five-member ring system consisting of four carbon atoms and one oxygen atom (see Fig. 1) is considered the building unit of vitamin B12 [16], furan

fatty acids [17], and conducting polymers [18]. Furan also plays an essential role in combustion chemistry as second-generation biofuels due to the potential for their large-scale production, *e.g.*, from complex biomass such as cellulose [19, 20].
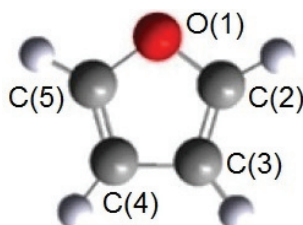

Fig. 1 – Schematic diagram of the furan molecule, C_4H_4O, showing labeling of the atoms.

Due to its natural occurrence in many biological and technological compounds, furan interaction with various forms of radiation has recently been the subject of intensive studies [21–27]. However, the hydrogen migration reaction has not yet been detected in furan, although theoretical calculations predict the possibility of its occurrence [28–30].

In the present study, the fragmentation of the gas-phase furan molecules in collisions with the H_3^+ and C^+ cations has been measured by exploiting *collision-induced emission spectroscopy* (CIES). In particular, the formation of the $OH(A^2\Sigma^+)$ radicals has been observed among other fragments. Because they are not structural components of furan molecules, observation of their $A^2\Sigma^+ \rightarrow X^2\Pi$ bands indicates the intramolecular hydrogen migration prior to the cation-induced dissociation. The present results show that the formation of excited $OH(A^2\Sigma^+)$ fragments depends on the particular projectile. The dissociation mechanism governing the $OH(A^2\Sigma^+)$ creation is explained.

2. EXPERIMENTAL METHOD

The experiments were performed at the University of Gdansk using a CIES spectrometer described recently in [31–33]. The schematic diagram of this spectrometer was presented in [34]. Hence only a brief discussion is presented here, combined with data relevant to furan and utilized projectiles.

The spectrometer was built with four independent parts, each fulfilling a different task. The first entity contained a vacuum chamber in which the ion source was mounted. It operated on a hot cathode discharge in different gases. This experiment used molecular hydrogen and methane to produce hydrogen and carbon ions. The ions produced were extracted from the plasma by applying 1000 V voltage. Then they were directed to the second unit containing a 60° magnetic mass selector. In the mass selector, ions were selected according to the *m/q* ratio. The appropriate energy of the cations was set using an electrostatic lens system, which

also directed them to the collision chamber. In the collision cell, each cation beam passed through furan vapors. Due to this interaction, furan became fragmented into ionized and neutral fragments. The luminescence of fragments was recorded using an optical spectrometer mounted in the last chamber. This assembly was equipped with a 1024 channel "Mepsicron" multi-channel photon detector connected to McPherson 218 spectrograph.

Emission lifetimes were estimated to be short enough to release all luminescence before leaving the collision cell. The collection of experimental data was performed by utilizing the 1200–l/mm grating. The OH luminescence was not intense and required long acquisition times. Thus due to time constraints, the high-resolution spectra with $\Delta\lambda = 0.4$ nm (FWHM) were only measured at the 1000 eV projectiles energy. At this energy, the cation beam current was 100 nA for H_3^+ and about 20 nA for C^+ in the collision region. The deficiency of the C^+ ion beam current was compensated by increasing the measurement time. It was set five times longer than the recording time using H_3^+. The background signal was measured by cutting off the furan beam and subtracted from the optical fragmentation spectra.

Furan was purchased from Sigma Aldrich. A declared purity was 99%. Furan is liquid but is highly volatile (at 25°C, the vapor pressure is 605.2 mmHg [35]). Thus it was applied without heating the sample. It was only degassed through several freeze-pump-thaw cycles. The pressure of furan was kept constant at 15 mTorr, as controlled by the Barocel capacitance manometer. It was also verified that the emission signal increased linearly with pressure up to 30 mTorr, implying a single collision regime.

3. RESULTS AND DISCUSSION

High-resolution optical fragmentation spectra measured for collisions between the H_3^+ and C^+ cations and furan molecules are shown in Fig. 2. Both spectra show spectral features of the molecular $OH(A^2\Sigma^+ \rightarrow X^2\Pi)$ $\Delta v = 0$, and $CH(C^2\Sigma^+ \rightarrow X^2\Pi_r)$ $\Delta v = 0$ bands. The spectrum obtained in the H_3^+ collisions (Fig. 2a) contains a much weaker signal than that obtained for C^+ impact (Fig. 2b). Moreover, the relative intensities of the features in both spectra are different.

It should be noted that optical fragmentation spectra for H^+, H_2^+, and He^+ ions were also measured. However, these were characterized by a poor signal-to-noise ratio. Therefore, no conclusion could be drawn from them, and these spectra were excluded from further analysis.

The $OH(A^2\Sigma^+ \rightarrow X^2\Pi)$ and $CH(C^2\Sigma^+ \rightarrow X^2\Pi_r)$ bands overlap, and it is challenging to draw correct conclusions from an analysis of the experimental results alone. Thus, theoretical spectra of these molecular bands were calculated to separate both features and recognize the differences in both collisional systems. The fittings were performed by comparing the experimental contours with simulated curves computed using the LIFBASE molecular spectra simulation package [36]. Rovibrational

spectroscopic constants of the $A^2\Sigma^+$, $X^2\Pi$ electronic states of OH [37–40], and $C^2\Sigma^+$, $X^2\Pi_r$ states of CH [41–43] were employed to calculate positions and intensities of spectral features. Moreover, the rovibrational populations were assumed to be Boltzmann.
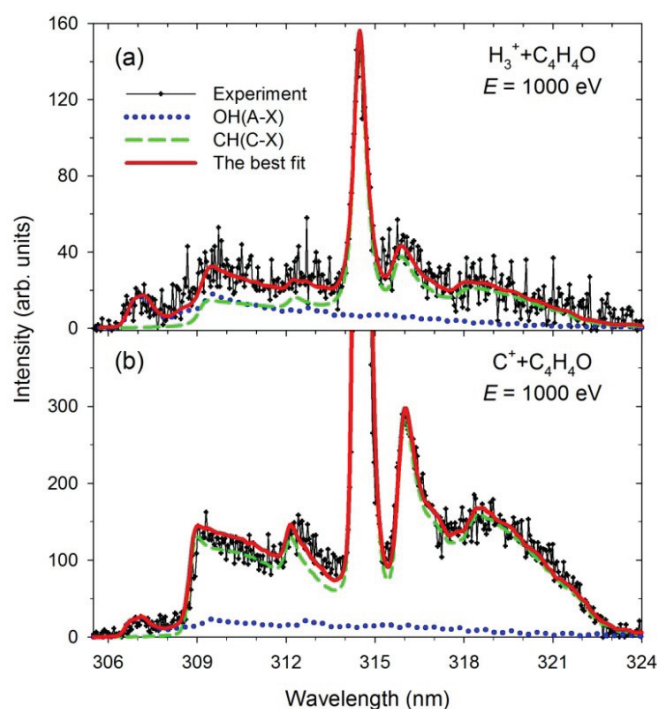

Fig. 2 – (Color online) The experimental (black dots) and simulated (red contours) $CH(C^2\Sigma^+\rightarrow X^2\Pi_r)$ + $OH(A^2\Sigma^+\rightarrow X^2\Pi)$ luminescence spectra obtained in the (a) H_3^+ + furan, (b) C^+ + furan at 1000 eV projectile energy.

In Fig. 2, solid red lines represent the $OH(A^2\Sigma^+\rightarrow X^2\Pi)$+$CH(C^2\Sigma^+\rightarrow X^2\Pi_r)$ best fits. These contours were obtained by employing the Voigt profile for the apparatus function with a resolution $\Delta\lambda$ of 0.45 and 0.42 nm (FWHM) for H_3^+ and C^+ cations, respectively. The program yields the characteristic vibrational (T_v) and rotational (T_R) temperatures listed in Table 1.

Table 1

Vibrational (T_v) and rotational (T_R) temperatures obtained from the fittings. The uncertainties were 500 K for T_v and T_R in both impact systems

Transition	H_3^+ + C_4H_4O		C^+ + C_4H_4O	
	T_v [K]	T_R [K]	T_v [K]	T_R [K]
$OH(A^2\Sigma^+\rightarrow X^2\Pi)$ $\Delta v = 0$	3900	4800	10000	12000
$CH(C^2\Sigma^+\rightarrow X^2\Pi_r)$ $\Delta v = 0$	4900	5500	5500	6000

The main feature in the 305–324 nm wavelength range is the $CH(C^2\Sigma^+ \rightarrow X^2\Pi_r)$ band (see [44]). Its emission (~308.5–324.0 nm) arises from electronic transitions from the $C^2\Sigma^+$ third excited to the $X^2\Pi_r$ ground electronic level with no change in the vibrational quantum number ($\Delta v = 0$). Computations show that vibrational transitions from this higher-lying electronic level generate characteristic spectral emission bands, with the strongest being related to the (0,0) band (314.5 nm). At 312 and 316 nm, the asymmetric peaks are produced by the overlapping R and P branches of the (1,1) vibrational transitions, respectively. Both spectra have the same major components, but their shapes vary due to different temperatures. The relative peak amplitudes of the (1,1) vibrational transitions depend on the vibrational temperature. Either T_v and T_R rise with increasing cation mass (see Table 1).

The $A^2\Sigma^+ \rightarrow X^2\Pi$ molecular band of the OH radical can only be distinguished when both contours are drawn. As shown in Fig. 2, the 305–308 nm spectral region displays an unhindered part of the band of this radical. Calculations show that the band head of the R branch of the (0,0) transitions produces the peaks at this spectral range. Other $\Delta v = 0$ transitions of the $OH(A^2\Sigma^+ \rightarrow X^2\Pi)$ overlaps with the $CH(C^2\Sigma^+ \rightarrow X^2\Pi_r)$ band. The rotational temperature determines the shape of a tail towards a higher wavelength corresponding to transitions between higher rotational levels. As seen in Table 1, both temperatures increase as the mass of the cation rises. T_v and T_R are twice as large in collisions with carbon ions as H_3^+.

The C^+ projectiles produced vibrationally and rotationally hotter CH and OH products than interactions with the H_3^+ cations, indicating different physical conditions during the collisions. Indeed, previous studies have shown that H^+, H_2^+, and H_3^+ do not induce effective fragmentation [26, 31–34] compared to heavier projectiles [27, 34, 45]. According to Alvarado *et al.* [46], the energy transferred to the target molecules is less for hydrogen beams than heavier projectiles because a lower electronic stopping characterizes the light cations. Thus H_3^+ projectiles traverse a low electron density and cannot efficiently induce collisional excitation of the electronic system of the target molecule [46]. In contrast, the electronic stopping of C^+ should be high enough to generate superexcited furan molecules [31]. This superexcitation of furan can trigger a cascade of further fundamental reactions, including its isomerization and fragmentation. In consequence, vibrational and rotational energy may readily be deposited into the reaction products in addition to electron excitation, thus giving the hotter fragments.

It can be seen that the total OH band intensity ratio to the CH band intensity decreases as the projectile mass rises. The I_{OH}/I_{CH} ratio obtained for the H_3^++furan collisions was found to be 0.40 and is more than four times higher than $I_{OH}/I_{CH} \sim 0.09$ ratio obtained for the C^++furan. Heavy ions cause more efficient fragmentation of the target molecules, while the isomerization process is less efficient due to relatively high energy barriers in their mechanisms [29]. Thus the increased production of CH fragments alters this ratio. This trend seems to occur commonly in various impact systems. The average relative abundances of individual excited fragments to the total emission calculated in the $H^+/H_2^+/He^+ + C_5H_5N$ and $H^+/H_2^+/H_3^+ + C_4H_8O$ collisions have recently shown that isomerization of pyridine occurred at a comparable

level in all collisional systems, but the CH production, in contrast, increased with a higher mass of cation [31].
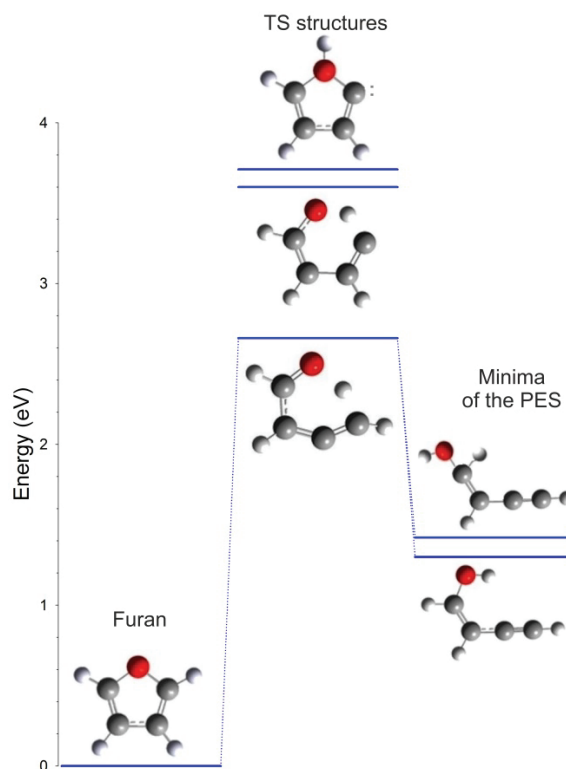

Fig. 3 – Schematic view of the dynamics of furan molecules isomerization. The drawing was developed using the values of relative energies, minima, and *transition state* (TS) structures of the *potential energy surface* (PES) for the isomerization of furan described in [29, 30].

Both C^+ and H_3^+ cations' kinetic energies are high enough to prompt a cascade of further elementary reactions [31–34, 45] *via* one of the five impact interactions, namely dissociative ionization, dissociative excitation, charge transfer, ion-molecule complex formation, direct dissociative excitation of a molecular projectile. In particular, the charge transfer mechanism is energetically the most favored reaction because it is usually exoergic [4, 26, 27, 31–34, 45]. A collisional interaction triggers the rearrangement of furan's geometrical structure since the spectroscopic marks for the existence of one of the furan isomerization channels are here observed. The most recent theoretical calculations of furan fragmentation have predicted some isomerization pathways accompanied by displacement of hydrogen atoms along the furan's ring [29, 30]. Both extended microcanonical metropolis Monte Carlo method [29] and the density functional theory [30] have shown that the 2,3-H shift has the lowest energy barrier [30], which is around 0.9 eV lower than 2,1-H and 3,4-H shifts. However, the production of OH in the dissociation of furan should proceed

through a reaction that develops OH at one end of the molecular open-chain able to detach by scission of the nearest O–C bond.

Figure 3 shows the most likely isomerization pathways leading to the production of such open-chain structures of furan. An H transfer from C(2) to O(1) is done through three transition state structures (TS structures in Fig. 3). The most promising mechanism in the OH formation involves the reaction pathway showing the lowest energy barrier located just 2.66 eV above furan canonical form and implies simultaneous 2,1- and 3,2-H shifts accompanied by a single C(2)–O(1) bond rupture (the lowest TS structure in Fig. 3). Then this transition state structure can rearrange into two minima of the PES, *i.e.*, stable alkyne−alcohol structures differing in energy by 0.12 eV [29]. Both open-ring molecules develop –OH side terminal, which can serve as the last step in OH release. The second transition state requires almost 1 eV more energy, and it occurs *via* an open-ring structure that does not include complex isomerization. This channel leads to relatively high-energy quasi-cyclic open isomers [29], not drawn in Fig. 3. The formation of closed-ring furan-$C_{2,1}$-carbene (the highest TS structure in Fig. 3) is less probable than open-ring isomers because its production must compete with the barrierless reaction of C–O bond fission [30].

4. SUMMARY

Modern computer techniques and increased computing power have allowed the rapid development of quantum-mechanical systems calculations. Different computational methods have recently been applied to calculate new furan fragmentation channels [29, 30]. In contrast to previous theoretical works, these calculations predict significant furan isomerization associated with the movement of hydrogen atoms alongside the furan's skeleton. Up to now, any of the suggested pathways have been observed to the best of our knowledge.

In the present work, the fragmentation of the gas-phase furan molecules in collisions with the low-energy cations has been measured exploiting collision-induced emission spectroscopy. In particular, the formation of the OH radicals has been identified among the fragmentation products. Because these radicals are not structural components of furan molecules, observation of their emission bands implies the intramolecular hydrogen migration prior to the cation-induced dissociation. The present results show that the cation-induced furan's isomerization occurs undeniably and depends on the particular projectile. Guided by the theoretical calculations mentioned above, the most likely scenario of furan's dissociation mechanism leading to the OH formation has been considered.

REFERENCES

1. N. G. Kling *et al.*, Nat. Commun. **10**, 2813 (2019).
2. M. McDonnell *et al.*, J. Phys. Chem. Lett. **11**, 6724−6729 (2020).
3. F. Ota *et al.*, Phys. Chem. Chem. Phys. **23**, 20174–20182 (2021).
4. T. J. Wasowicz, B. Pranszke, J. Phys. Chem. A **120**, 964 (2016).
5. M. Zubek *et al.*, J. Chem. Phys. **141,** 064301 (2014).
6. T. J. Wasowicz *et al.*, J. Phys. B: At. Mol. Opt. Phys. **50,** 015101 (2017).
7. H. Xu *et al.*, J. Chem. Phys. **133**, 071103 (2010).
8. Y. H. Jiang *et al.*, Phys. Rev. Lett. **105**, 263002 (2010).
9. S. Maclot *et al.*, J. Phys. Chem. Lett. **4**, 3903−3909 (2013).
10. S. Oberli *et al.*, Phys. Chem. Chem. Phys., **21,** 25626–25634 (2019).
11. T. J. Wasowicz *et al.*, J. Phys. B: At. Mol. Opt. Phys. **47**, 055103 (2014).
12. I. Linert *et al.*, Chem. Phys. Lett. **498**, 27−31 (2010).
13. T. J. Wasowicz *et al.*, Photon. Lett. Pol. **3,** 110 (2011).
14. A. Ratkiewicz, React. Kinet. Mech. Catal. **108**, 545−564 (2013).
15. D. R. Killelea *et al.* Science **319**, 790−793 (2008).
16. C. O. Kappe *et al.*, Tetrahedron **53**, 14179 (1997).
17. F. D. Gunstone *et al.*, J. Chem. Soc. Chem. Commun. **16**, 630–631 (1976).
18. S. Glenis *et al.*, J. Am. Chem. Soc. **115**, 12519 (1993).
19. M. Mascal, E. B. Nikitin, Angew. Chem.-Int. Ed. **47**, 7924 (2008).
20. Y. Roman-Leshkov *et al.*, Nature **447**, 982 (2007).
21. O. Sorkhabi *et al.*, J. Chem. Phys. **111**, 100 (1999).
22. E.E. Rennie *et al.*, Chem. Phys. **236**, 365–385 (1998).
23. Z.D. Pešić *et al.*, Phys. Rev. A **82**, 013401 (2010).
24. T. J. Wasowicz, B. Pranszke, J. Phys. Conf. Ser. **635**, 032055 (2015).
25. M. Dampc *et al.*, J. Phys. B: At. Mol. Opt. Phys. **48**, 165202 (2015).
26. T.J. Wasowicz, B. Pranszke, Eur. Phys. J. D **70** (8) 175 (2016).
27. T.J. Wasowicz *et al.*, Int. J. Mol. Sci. **20**, 6022 (2019).
28. K. Sendt *et al.*, J. Phys. Chem. A **104**, 1861−1875 (2000).
29. E. Erdmann *et al.*, J. Phys. Chem. A **122**, 4153−4166 (2018).
30. T. Li *et al.*, Energy Fuels **35**, 7819−7832 (2021).
31. T.J. Wasowicz, Int. J. Mol. Sci. **23**, 205 (2022).
32. T.J. Wasowicz, Rom. Rep. Phys. **73**, 203 (2021).
33. T.J. Wasowicz, B. Pranszke, Acta Phys. Pol. A **140**, 228 (2021).
34. T.J. Wasowicz, B. Pranszke, J. Phys. Chem. A **119** (4) 581 (2015).
35. CSID:7738, http://www.chemspider.com/Chemical-Structure.7738.html (accessed 09:49, February 07, 2022).
36. J. Luque, D. R. Crosley, Lifbase: Database and Spectral Simulation (Version 1.5), SRI International Report MP 99-009. 1999. Available online: https://www.sri.com/case-studies/lifbase-spectroscopy-tool/ (accessed on 29 October 2021).
37. J. Luque, D.R. Crosley, J. Chem. Phys. **109**, 439 (1998).
38. J. Brzozowski *et al.*, Phys. Scripta **17**, 507 (1978).
39. K.R. German, J. Chem. Phys. **63**, 5252 (1975).
40. K.R. Steffens *et al.*, J. Chem. Phys., **106**, (1997).
41. J. Brzozowski *et al.*, Astrophys. J. **207**, 414 (1976).
42. W. Ubachs *et al.*, J. Chem.Phys. **84**, 3032 (1986).
43. J.B. Jeffries *et al.*, J. Quant. Spectrosc. Radiat. Transf. **37**, 419 (1989).
44. A. M. Bass, H. P. Broida, A spectrophotometric atlas of the spectrum of CH from 3000 A to 5000 Å, U.S. Department of Commerce, National Bureau of Standards Monograph 24, (1961).
45. T. J. Wasowicz, Res. Phys. **18**, 103244 (2020).
46. F. Alvarado *et al.*, Phys. Chem. Chem. Phys. **8**, 1922–1928 (2006).